JOURNAL OF PROPULSION AND POWER
Vol. 26, No. 2, March–April 2010

Effect of Swirl on Shock Structure in Underexpanded Supersonic Airflow

A. Abdelhafez* and A. K. Gupta†
University of Maryland, College Park, Maryland 20742

DOI: 10.2514/1.45716

This study examines the effect of imparting swirl to underexpanded supersonic-nozzle airflow on shock structure under matched mass flow conditions. A convergent nozzle with swirling capabilities is used to generate the underexpanded airflow. Fuel is injected coaxially at the nozzle throat. Nonreacting conditions are considered, wherein fuel is simulated by mixtures of helium, argon, and krypton inert gases. It was found that the effects of swirl and nozzle reservoir pressure interfere destructively from the point of view of shock-structure axial compactness. Increasing reservoir pressure stretches the shock structure axially, whereas swirl shrinks it. On the other hand, constructive interference was observed from the point of view of radial jet expansion; both result in greater jet diameter. The application of swirl was found to weaken the shock structure at matched reservoir pressure but to strengthen it at matched mass flow. It was also found that fuel injected at low subsonic Mach numbers into the supersonic airflow has to propagate initially with a negative shear angle; i.e., the cross-sectional area of fuel-rich core flow converges first, before this core flow reaches a throat after which it propagates supersonically. This behavior was found to be advantageous, as it results in reduced shock-structure strength.

Nomenclature

a	=	speed of sound
D	=	nozzle exit diameter (11 mm)
DR	=	air/fuel density ratio at injection plane
M_c	=	convective Mach number
M_{rel}	=	air/fuel relative Mach number at injection plane
p	=	pressure
S	=	swirl number
v	=	velocity
z	=	axial coordinate
γ	=	ratio of specific heats

Subscripts

a	=	axial
t	=	tangential

I. Introduction

SWIRLING flow in nozzles occurs in a number of important propulsion applications, including turbofans and turbojet engines, spin-stabilized rockets, and integral rocket/ramjets. In the first two cases, the tangential velocity component is induced by the motion of turbine blades and by the rocket spin, respectively. For ramjets, experimental studies [1] have demonstrated that swirl generated by fixed vanes located in the dump combustor inlet can lead to significantly improved combustor performance. Clearly, the generated swirl in each of those propulsion systems will persist at some level to the inlet of the exhaust nozzle. Therefore, it is important to examine the effect of the tangential velocity component on nozzle flowfield, so that design parameters such as thrust and mass flow rate can be accurately determined.

Received 30 May 2009; revision received 2 November 2009; accepted for publication 10 November 2009.

*Graduate Student, Department of Mechanical Engineering, 2181 Glenn Martin Hall. Student Member AIAA.

†Distinguished University Professor, Department of Mechanical Engineering, 2181 Glenn Martin Hall. Fellow AIAA.

The structure of highly underexpanded nozzle jets was investigated experimentally and analytically by Adamson and Nicholls [2], who presented a method for calculating the position of the first Mach disk. In their calculation, the axial pressure distribution on the flow centerline downstream of the nozzle exit (calculated by method of characteristics) was used to define a fictitious nozzle extension. The Mach disk was then assumed to exist at the point at which atmospheric pressure would be attained upstream of the disk; i.e., the disk was assumed to exist at the end of a fictitious nozzle extension. Physical arguments were employed to extend the analysis to nozzles with supersonic exit Mach numbers. An approximate method for computing the jet boundary, up to the point of maximum jet area, was also given. The analytical results compared favorably with experimental data at relatively low nozzle pressure ratios.

Lewis and Carlson [3] experimentally determined the distance from the nozzle exit plane to the first Mach disc in gas-only and gas–particle jets issuing from underexpanded supersonic nozzles. An empirical correlation of the data was presented that is valid for both jet types and incorporates the effect of gas specific-heat ratio. In a relevant experimental investigation, Crist et al. [4] studied the structure of underexpanded jets with stagnation pressures up to 15,000 psia, ambient pressures down to 100 μHg, and stagnation temperatures up to 4200 K. The location of the first Mach disk was found to be insensitive to the ratio of specific heats, nozzle-lip geometry, and absolute pressure. For overall pressure ratios up to about 3×10^5 (i.e., ratio of reservoir to freestream static pressures), the location of Mach disk was found to vary as the square root of overall pressure ratio. The diameters of the Mach disk, jet boundary, and intercepting shock were found to increase with decrease in specific-heat ratio and to decrease at high stagnation density, where intermolecular forces become important. At high pressure ratios, the ratio of Mach-disk diameter to Mach-disk position appeared to be constant for a given gas. It was also found that the properties along the jet axis can be approximated by the properties of a flow through a hypothetical conical nozzle for which the half-angle is given as a function of specific-heat ratio. A simplified expression for the distribution of Mach number along the jet axis was given to good approximation as a function of specific-heat ratio.

Gostintsev et al. [5] studied an underexpanded supersonic swirling gas jet issuing from a convergent nozzle. They showed that the effect of rotation on the wave structure of an axisymmetric jet is qualitatively analogous to the effect of reduction in overpressure ratio. Using formulas for spiral isentropic flow, an approximate expression was obtained for estimating the location of the first Mach

disc in the swirling flow downstream of the nozzle exit. Batson and Sforzini [6] also studied the structure of swirling flow through a convergent nozzle, with emphasis on the effect of swirl on the flowfield, thrust, and mass flow produced by nozzled devices, such as jet engines and spin-stabilized rockets. It was reported that the axial velocity component increases, whereas the tangential one decreases, as the flow passes through the nozzle throat.

Vortex enhancement of supersonic mixing was studied experimentally by Settles [7]. Swirl was used to enhance shear-layer growth and mixing. It was concluded that swirl enhances compressible mixing; the degree of enhancement increases with increasing swirl. Settles also reported that the effects of convective Mach number and density ratio on the enhancement effect of swirl are still unknown and were thus recommended for future work.

In an experimental investigation, which is very pertinent to this current study, Lee et al. [8] examined the near-field flow structure of underexpanded coaxial swirl jets. Swirl streams were issued from a secondary annular nozzle, and a primary inner nozzle provided the underexpanded free jets. The interactions between the annular swirl and the underexpanded core jets were examined to quantify the effects of the former on the latter. It was shown that the presence of an annular swirl stream causes the core-flow Mach disc to move further downstream, with an increased diameter. In another pertinent study, Lee et al. [9] investigated the effect of nozzle inlet configuration on underexpanded swirling jets, which were generated by a convergent nozzle with four tangential inlets at the supply chamber. The nozzle inlet configuration was modified by using different plugs, holes, and needles, which were also used for measuring the flow properties at the nozzle inlet. The experimental results showed that the presence of a coaxial needle inside the nozzle supply chamber controls the properties of generated underexpanded swirling jets. The structures of these jet flows are highly dependent on the detailed configuration of the nozzle supply chamber.

Murakami and Papamoschou [10] examined the flow structure and mixing enhancement in 2-D and axisymmetric supersonic jets surrounded by secondary annular subsonic coaxial jets. The supersonic jets were issued from a convergent–divergent nozzle operated at offdesign (i.e., underexpanded or overexpanded) conditions. It was shown that the mixing enhancement using secondary parallel injection (referred to as MESPI by the researchers) halves the length of the potential core in both round and 2-D jets. A short distance past the potential core, mixing enhancement caused a reduction in centerline Mach number by 30% in round jets and 20% in 2-D jets. The corresponding reduction in peak molar concentration of a scalar injected in the primary flow was 65% in round jets and around 40% in 2-D jets.

Increased molecular mixing between fuel and oxidizer is essential for efficient combustion, which can be accomplished by increasing the turbulent mixing. It is now well known that large-scale coherent structures play an important role in incompressible turbulent mixing layers [11]. These structures engulf surrounding unmixed fluid and carry it into the mixing layer. Furthermore, it is possible that two adjacent vortical structures roll up upon one another, creating one larger structure, which leads to spreading of the mixing layer [12]. These two processes are believed to be fundamental for turbulent mixing in incompressible mixing layers.

Studies of compressible shear layers have shown that large-scale structures are similarly important in compressible turbulent mixing, changing its nature with convective Mach number [13–16]. It was found that the visual growth rate of a compressible shear layer with almost unity convective Mach number was only one-fourth of the growth rate of an incompressible mixing layer having the same freestream velocity and density ratios, regardless of the values of these ratios [13]. Moreover, it is known that supersonic shear layers are highly stable [17], limiting the desired mixing of fuel and oxidizer. It was predicted that a supersonic shear layer will be completely stable if the Mach number based on the relative speed exceeds 2.83, assuming an infinitely thin vortex sheet. This predicted stable nature of supersonic mixing layers has been later observed both in experiments [13,18] and in numerical simulations [19].

The flow of supersonic swirling jets in a stagnant atmosphere was further investigated by Cutler et al. [20], Cutler and Levey [21], and Levey [22]. The swirling jets were created by tangential injection into a swirl chamber and accelerated through a convergent–divergent nozzle. The researchers observed higher peak helix angles than previous studies, as well as lower densities and pressures along the jet axis. They found that the growth rates of mixing layer increased considerably with swirl. Moreover, when the swirling jets were operated overexpanded, unstable shock interactions produced vortex breakdown.

This work provides an experimental/numerical investigation, in which the effect of imparting swirl to underexpanded supersonic-nozzle airflow on shock structure is examined. Matched mass flow conditions are considered here. The effect of swirl has not been fully quantified in the literature yet, due to the inherent three-dimensionality of the problem. A convergent nozzle with swirling capabilities is used to generate the underexpanded airflow. Fuel is injected coaxially at the nozzle throat. Nonreacting conditions are considered, wherein fuel is simulated by mixtures of helium, argon, and krypton inert gases. Analyses are made of the effects of relative Mach number and density ratio across the air/fuel shear layer. The effects of these parameters on shock structure are investigated under both nonswirling and swirling conditions. Select cases have been chosen for a further analysis of the effect of convective Mach number on shear-layer growth.

II. Experimental Setup

The experimental investigation of this present work has been performed at the University of Maryland supersonic facility. The used supersonic-nozzle assembly is shown schematically in Fig. 1. A convergent nozzle with an effective inlet-to-exit area ratio of 25 is used to generate an underexpanded supersonic airflow. Reservoir pressures of up to about 9 atm (abs) are available, yielding near-field Mach numbers of up to 2.2 under nonswirling conditions. The nozzle has swirling capabilities, wherein the axial-tangential-entry technique with four tangential inlets is used to accurately control the degree of swirl imparted to airflow. This technique has been proven in previous research to be an efficient method for generating supersonic swirling jets [23–25]. Thermal flow meters/controllers are used to meter the flow rates of axial and tangential air components with an accuracy of $\pm 1.5\%$ of full scale.

The nozzle was machined out of a single aluminum rod. Aluminum was preferred to stainless steel because the former has higher thermal conductivity, which prevents overheating of the nozzle walls during combustion experiments. The higher conductivity allows radiated heat to be dissipated effectively through the thick nozzle walls. The dissipated heat is removed by forced convection of the entrained ambient cold air through the large surface area of nozzle external walls. The thickness of the nozzle lip was optimized to allow for significant entrainment of ambient air while having adequate rigidity for machining the exit section to the desired surface finish and dimensional tolerance.

A coaxial fuel-injection system is used to inject fuel along the axis of the air nozzle. A support flange upstream of the nozzle ensures and maintains concentricity of the fuel injection system with respect to the air nozzle, especially under swirling conditions. This flange comprises a conical sleeve that embraces the injection system. The sleeve wall thickness decreases in the direction of flow to provide streamlined performance and prevent any blockage close to the nozzle exit. The sleeve is held in place by three spokes extending to the support flange. Their thicknesses have been optimized to provide rigidity with minimum blockage to the incoming axial component of airflow. It should be noted here that those spokes are located physically upstream of the air tangential inlets and do not affect the flowfield of the tangential air component. Some wakes are expected to exist in the axial-component flowfield behind the spokes, but the supersonic flow exiting the nozzle was found to be fully axisymmetric with and without swirl.

The nanosecond schlieren diagnostic technique was used to visualize the shock structure in this study. schlieren imaging yields

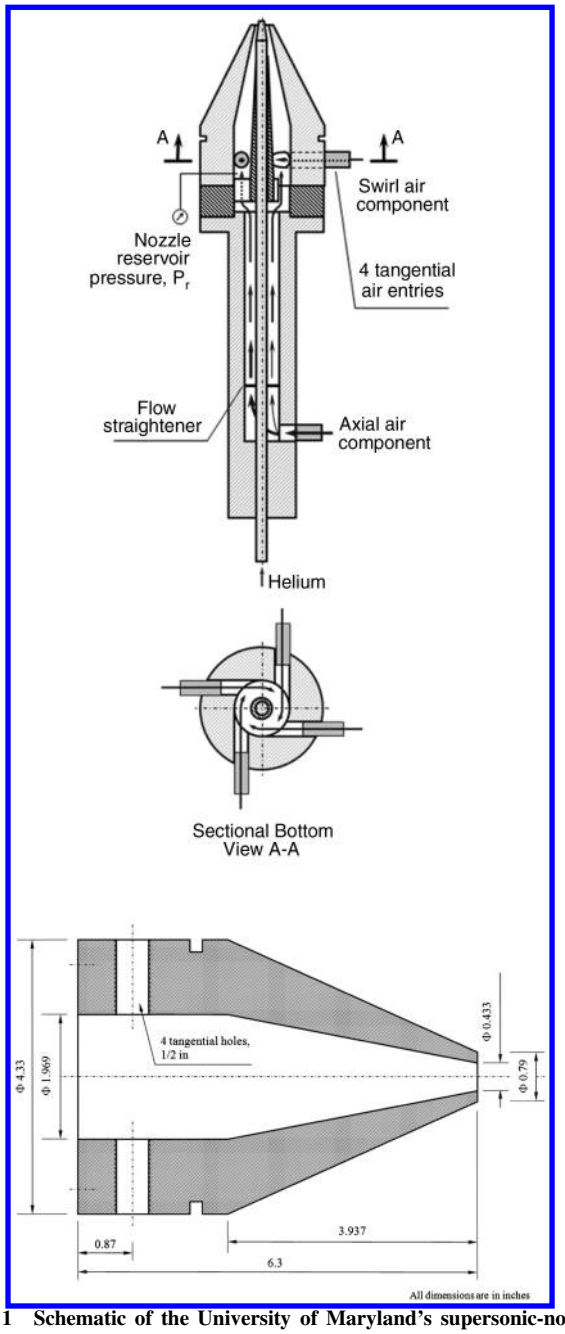

Fig. 1 Schematic of the University of Maryland's supersonic-nozzle assembly.

the first derivative of the refractive index in the test region, thus giving an estimate of the density gradients within the flowfield. The intensity of captured light can be further processed using image-processing techniques to obtain more quantitative information of the shock structure. Figure 2 shows a schematic of the used setup.

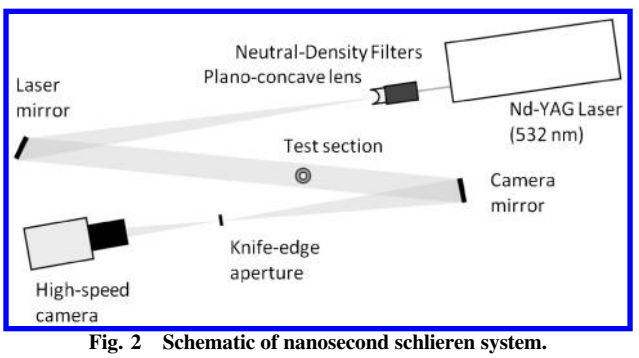

Fig. 2 Schematic of nanosecond schlieren system.

The light source is a 532-nm Q-switched Nd:YAG laser with pulse duration of only 5 ns, which explains the term *nanosecond schlieren* and makes this setup unique compared with conventional schlieren setups. The nanosecond light duration allows for capturing instantaneous images of the flowfield. No fluctuations are thus accumulated or averaged on the image, which allows for accurate visualization of the shock structure.

Because of the fact that the intensity of laser light is too high for safe camera operation, the laser was equipped with neutral-density

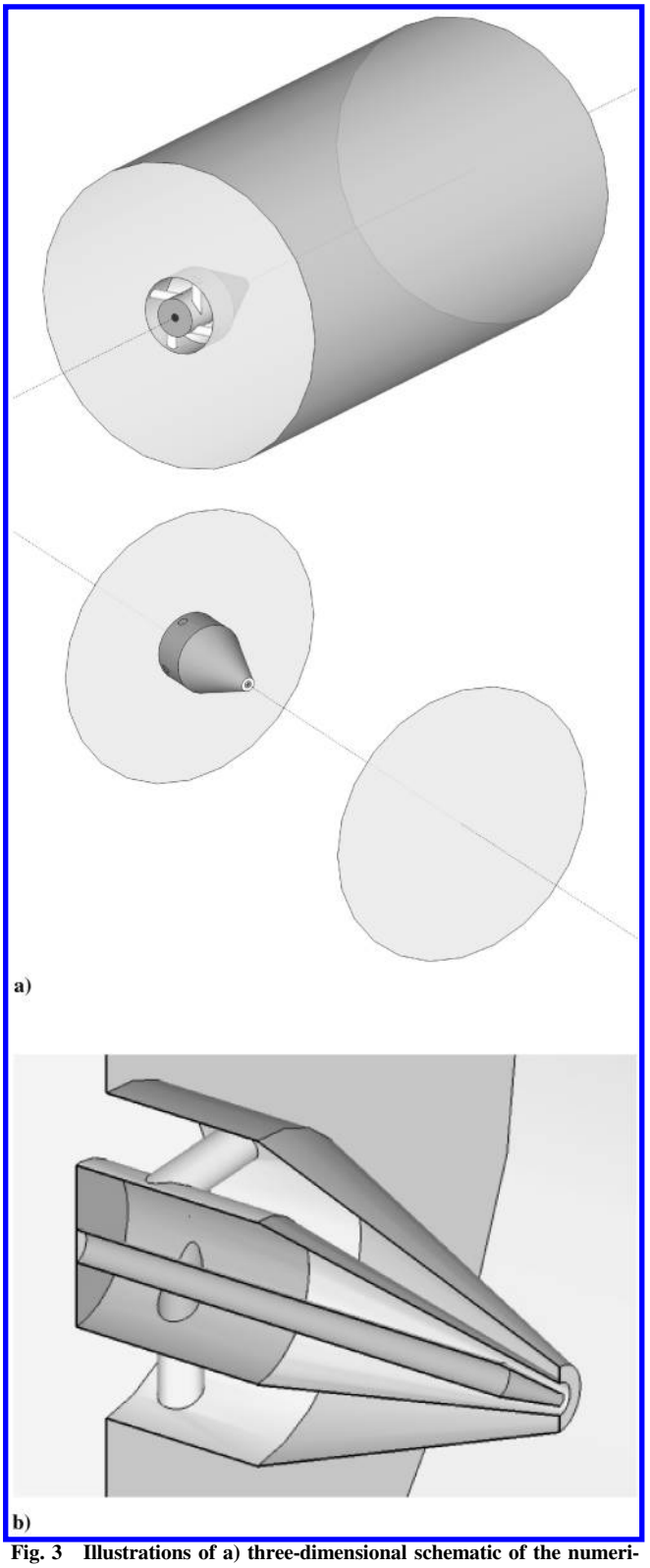

Fig. 3 Illustrations of a) three-dimensional schematic of the numerically simulated geometry and b) zoom-in cutaway highlighting the nozzle details.

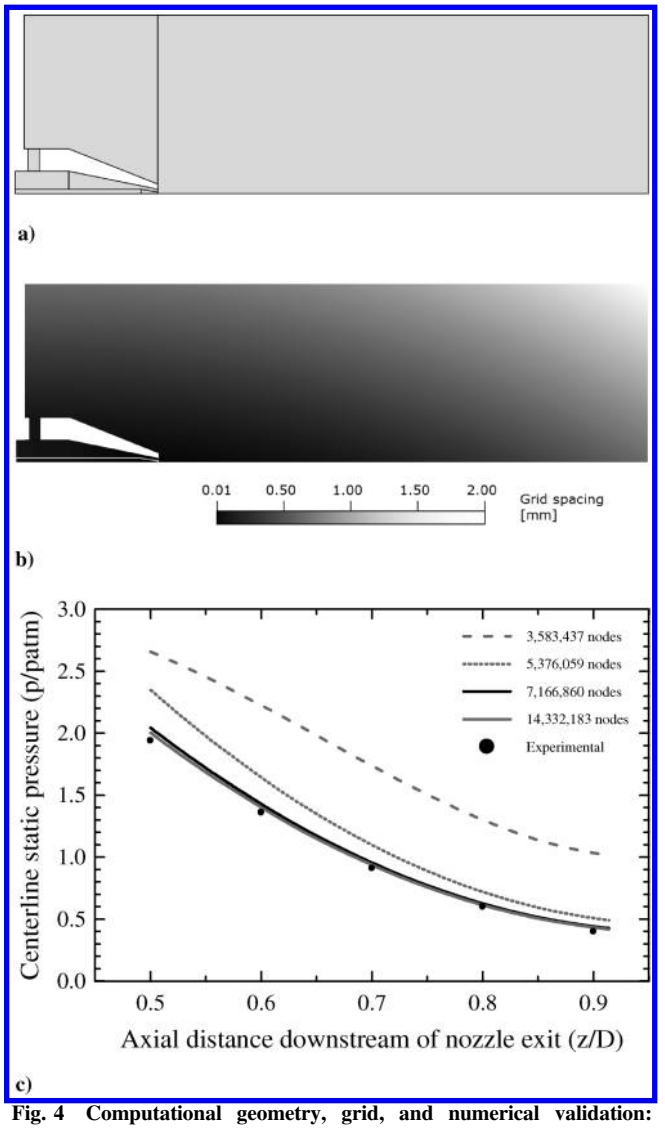

Fig. 4 Computational geometry, grid, and numerical validation: a) individual subvolumes of the simulated geometry, b) grid spacing within the center plane, and c) mesh dependence and validation of numerical code (case 0s1).

filters that reduce its light intensity. The divergence of the collimated beam is then increased by means of a plano-concave lens. The divergent beam fully illuminates a concave mirror, which reflects the light in a collimated fashion through the test section. This is essential for avoiding a skewed perspective of the flowfield. After penetrating the flow, the light is focused by another concave mirror. A knife-edge aperture intercepts the light at the focal point of the second mirror to fulfill the schlieren principles. The resulting images are then captured at a resolution of 1024×1024 pixels using a high-speed camera that is synchronized with the laser.

III. Numerical Simulation Type and Assumptions

The commercial CFD-FASTRAN[‡] 2008 hybrid large eddy simulation (LES) and Reynolds-averaged Navier–Stokes (RANS) code, provided by ESI-Group, was used for all the simulations conducted in this study. Since a free supersonic flow is involved, special emphasis was placed on the choice of boundary conditions that represent the flow surroundings. The entire nozzle assembly was surrounded by a cylindrical enclosure of $40D$ diameter and $70D$ length, where D is the nozzle exit diameter [11 mm, a good representation of jet size (see Fig. 3)]. The $40D$ enclosure diameter ensures that the side boundaries are far enough from the jet to eliminate any interference of both and to maintain constant near-stagnation atmospheric properties at the boundaries. Consequently, the bottom and side enclosure surfaces were assigned the fixed-pressure boundary condition, which matches the constant actual atmospheric ambient pressure. The top side of the enclosure, on the other hand, is an extrapolated outlet located $55D$ away from the nozzle exit ($\approx$78% of the $70D$ enclosure length). This guarantees that the flow leaves the simulated geometry shock-wave-free, since it was observed experimentally that complete transition to subsonic speeds occurs about $30D$ downstream of the nozzle exit.

Axisymmetry was enforced; i.e., only one quadrant of the geometry depicted in Fig. 3 was simulated. Special emphasis was placed on the level of cell skewness. The simulated geometry was subdivided into individual volumes, each meshed separately, to keep the skewness level of the most skewed cell below 0.5 (see Fig. 4a). A variable-size grid was generated with tetrahedral cells and a grid spacing ranging from 0.01 to 2.0 mm (see Fig. 4b). Grid spacing is defined here as the longest edge of the cell. Tighter meshing was implemented near and at the critical geometry locations: e.g., the exits of the nozzle and fuel-injection system. Mesh dependence was carefully examined through testing multiple levels of mesh tightness (see Fig. 4c). A total of 7,166,860 nodes per quadrant yielded the desired accuracy. Higher tightness levels did not result in significant accuracy enhancement and were thus not considered, to optimize the computational time.

Four subgrid RANS turbulence models from the FASTRAN library were tested for their capabilities to accurately predict a free swirling supersonic jet: namely, the k-ε, k-ω, Spalart–Almaras, and Baldwin–Lomax [26] models. The parameters of each model were optimized to yield the least rms error, when compared with experi-

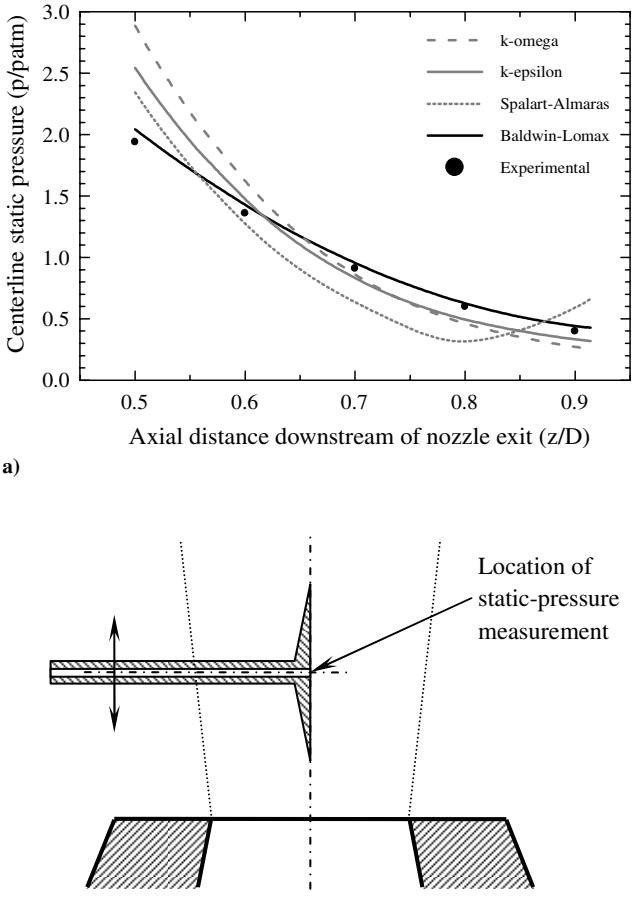

Fig. 5 Choice of turbulence model and location of static pressure measurement: a) choice of RANS turbulence model (case 0s1) and b) schematic presentation of how the centerline static pressure was measured experimentally for the sake of code validation.

[‡]Data available online at http://www.esi-group.com/products/Fluid-Dynamics/cfd-fastran [retrieved May 2009].

mental data within the near-field supersonic flowfield up to $5D$ downstream of the nozzle exit. Figure 5 compares the obtained centerline static-pressure trace of each model to the corresponding experimental data. It can be clearly seen that the Baldwin–Lomax model offers the best agreement with experimental data among the available models within the FASTRAN code. Although several modifications of the Baldwin–Lomax model have been published, in an attempt to enhance its prediction capabilities, it should be noted here that FASTRAN is not an open-source code and none of those modifications are available. Nevertheless, the obtained degree of accuracy with the basic Baldwin–Lomax model was considered acceptable for the scope of this study.

Calculation of the viscosity and conductivity was based on the kinetic theory of gases. A turbulent Schmidt number of 0.9 was used, and the mass diffusivity was calculated based on Fick's law with a Schmidt number of 0.5. A turbulent Prandtl number of 0.9 was used for calculating the turbulent conductivity. Similar to the experimental conditions, the total temperature at the air inlets was kept fixed at 300 K, and the total pressure was maintained at 7.91 bar for the nonswirling cases and 8.82 bar for the swirling cases. The 8.82 bar value was carefully chosen to ensure a common air flow rate of 175 g/s. The need for higher nozzle reservoir pressure with swirl was explained in detail in the work of Abdelhafez and Gupta [27]. The total pressure and temperature at the air inlets were preserved throughout the iteration process in each examined case until convergence was attained. Owing to the relatively large cross-sectional areas of the air inlets, the entrance velocity of air was only 9.7 m/s, resulting in almost identical inlet stagnation and static conditions.

The nozzle walls were set to be isothermal at 280 K, based on multiple temperature measurements of the nozzle interior and exterior walls. This is attributed to the aforementioned fact that the nozzle is made of aluminum, which has a high thermal conductivity and thus allows the nozzle to act as a near-isothermal body. The walls of the fuel-injection system, on the other hand, were set to be adiabatic, because the injection system is immersed almost totally into the nozzle and conditioning chamber, which allows for negligible amounts of heat to be conducted axially upstream through the thin walls of fuel system. Moreover, it is made of stainless steel that has a much lower thermal conductivity (relative to aluminum).

The initial conditions of simulation were set for all cases at 1 atm static pressure, 300 K static temperature, 9.7 m/s axial velocity, and zero radial and tangential velocities. Consequently, the simulation incorporated the transient behavior as the high-pressure air expands and marches from the geometry inlet to the exit. An initial Courant–Friedrichs–Lewy number [28] of 0.1 was chosen that increases to unity as convergence is approached. Time integration is implicit; a point Jacobi scheme was used, and a backward Euler discretization was implemented. Each case included 20,000 iterations. Convergence to 10^{-6} residuals was usually attained after 18,500–19,500 iterations.

IV. Test Matrix

The effect of swirl is investigated here by forwarding the entire airflow to nozzle tangential entries. This allows for examining a single degree of swirl: namely, the maximum attainable one. Following a definition used for incompressible swirling jets [23,29], a nozzle-based geometrical swirl number S_g is defined for air as

$$S_g = \left(\frac{\pi r_o R_o}{A_t}\right)\frac{m_t}{m_a + m_t} \tag{1}$$

where $(\pi r_o R_o/A_t) = 0.68$ for the geometry of used nozzle and its tangential entries, and m_a and m_t are the axial and tangential components of airflow, respectively. Consequently, all swirling cases of this study have the same nozzle-based geometrical swirl number of 0.68. The term *nozzle-based* refers to nozzle operation in the absence of coaxial injection system, as the presence of this system reduces the geometrical swirl number down to 0.36 [30]. This significant reduction made the examination of the effect of swirl feasible only at its maximum attainable degree.

In addition to an extensive examination of the effect of swirl on the shock structure, the effects of two flow parameters are investigated here under both nonswirling and swirling conditions: namely, the relative Mach number M_{rel} and air/fuel density ratio DR. The former is defined here as

Table 1 Test matrix[a]

Case[b]	Injected gas	M_{rel}	DR	Experimental	Numerical
0, 0s1[c]	——	——	——	——	——
	Effect of relative Mach number				
1, 1s	Helium	0.44	35.50	✓	✓
2, 2s	Helium	0.41	35.50	✓	——
3, 3s	Helium	0.39	35.50	✓	——
4, 4s	Helium	0.37	35.50	✓	——
5, 5s	Helium	0.35	35.50	✓	✓
6, 6s	Helium	0.32	35.50	✓	——
7, 7s	Helium	0.30	35.50	✓	——
8, 8s	Helium	0.28	35.50	✓	——
9, 9s	Helium	0.26	35.50	✓	✓
10, 10s1	Helium	0.21	35.50	——	✓
11, 11s	Helium	0.00	35.50	——	✓
12, 12s	Helium	−0.21	35.50	——	✓
13, 13s	Helium	−0.48	35.50	——	✓
	Effect of density ratio				
14, 14s	100% helium	0.21	35.50	——	✓
15, 15s	80% helium/20% argon	0.21	12.68	✓	✓
16, 16s	70% helium/30% argon	0.21	9.60	✓	——
17, 17s	60% helium/40% argon	0.21	7.72	✓	——
18, 18s	50% helium/50% argon	0.21	6.46	✓	✓
19, 19s	40% helium/60% argon	0.21	5.55	✓	——
20, 20s1	30% helium/70% argon	0.21	4.86	✓	——
21, 21s	20% helium/80% argon	0.21	4.33	✓	✓
22, 22s	50% helium/50% krypton	0.21	3.24	——	✓
23, 23s	50% argon/50% krypton	0.21	2.29	——	✓

[a]Constant parameters are air total temperature of 300 K at the inlet and nozzle reservoir pressure of 7.91 bar (nonswirling) and 8.82 bar (swirling).
[b]Geometrical swirl number for swirling cases is $S_g = 0.36$.
[c]Air only; no fuel injection.

$$M_{\text{rel}} = \frac{v_{\text{air}} - v_{\text{fuel}}}{0.5(a_{\text{air}} + a_{\text{fuel}})} \quad (2)$$

This definition relates the difference in freestream velocities between fuel and air to the average speed of sound. It should be noted that the fuel simulant is injected here at velocities smaller than the sonic velocity of airflow in most examined cases. Therefore, v_{fuel} is subtracted from v_{air} in the above definition, in order for M_{rel} to have positive values. Nevertheless, in a few extreme cases, the fuel simulant is injected at velocities greater than those of the airflow, and the corresponding values of M_{rel} are indicated here without neglecting their negative signs, to highlight the unique nature of those cases: i.e., $v_{\text{fuel}} > v_{\text{air}}$.

Each examined case in this study has a nominal value of M_{rel} that describes the injection conditions within that case. Since all cases to be presented here use no recess (i.e., fuel is injected at the throat of the air nozzle), the nominal value of M_{rel} was calculated for each case using the fuel-injection velocity and the sonic (throat) value of v_{air}. A comparison based on nominal M_{rel} thus allows for examining the effect of fuel-injection conditions on shock structure. Such analysis should not be confused with the shear-layer-specific analysis of the effect of convective Mach number M_c on shear-layer properties (to be presented in this study as well). Under nonswirling conditions, sonic v_{air} was found to be 323 m/s, based on isentropic ideal-gas relations. No similar simple calculations of v_{air} could be carried out for the swirling cases, due to the intrinsic three-dimensionality of swirling flows. Nevertheless, the results of numerical simulations revealed that the magnitude of sonic v_{air} is 329 m/s with swirl, which is almost equal to the nonswirling value. This fact allowed for examining the same nominal values of M_{rel} under both nonswirling and swirling conditions in this study.

The shock structure and all properties of the airflow, including the aforementioned values of v_{air}, depend on air total pressure and temperature. Both were kept constant at 7.91 bar and 300 K, respectively, for all nonswirling cases presented in this study, which resulted in a fixed air flow rate of 175 g/s. It was noticed, however, that imparting swirl to the airflow at the same nozzle reservoir pressure of 7.91 bar results in a reduced mass flow rate through the nozzle. This observation agrees with the findings of many previous studies (refer to [27] for an extensive review). It was proven that imparting swirl to the airflow results in additional choking of the nozzle: i.e., a lower mass flow rate compared with the corresponding nonswirling conditions at the same reservoir pressure. A theoretical limit of no flow was even predicted at an infinitely large swirl number. Therefore, a higher reservoir pressure is necessary to maintain the same flow rate through the nozzle. It was found in this study that a value of 8.82 bar yields identical air flow rates of 175 g/s in the nonswirling and swirling cases.

Table 1 lists the test matrix for the results presented here. A total of 48 cases are examined (24 nonswirling cases plus their swirling counterparts). Case pair 0 uses no fuel injection and serves for quantifying the effect of swirl on the supersonic flowfield and shock strength. Case pairs 1–13 study the effect of M_{rel}, wherein the injectant is helium. The injection velocity of helium is changed to induce different values of nominal M_{rel}. The effect of DR is studied through case pairs 14–23, wherein the injectant comprises different inert-gas mixtures. The mixture composition is varied to change mixture density and, consequently, DR. To maintain constant M_{rel} throughout the DR analysis, the injection velocity was adjusted to account for the changes in a_{fuel} due to the varying injectant composition. The values to be examined in both analyses of M_{rel} and DR were carefully selected according to the following criteria:

1) The experimentally attainable ranges are spanned with narrow intervals, to quantify the examined effects accurately. For example, M_{rel} is examined over the range 0.44–0.26 with eight intervals, and DR is covered in the range 12.68–4.33 with six intervals.

2) The numerical simulations span the experimental ranges with wide intervals: i.e., one simulation at the beginning of the range, one in the middle, and one at the end. Case pairs 1, 5, and 9 within the M_{rel} analysis, for example, were examined both experimentally and numerically. The same applies for case pairs 15, 18, and 21 within the DR analysis.

3) The numerical simulations extend beyond the experimental ranges to broaden the scope of the analysis and qualitatively examine how accurate the experimental trends would be when extrapolated beyond the ranges in which they were obtained.

Note that case pairs 10 and 14 (Table 1) are identical, as they have the same fuel simulant (helium), M_{rel}, and DR. These two case pairs link the analyses of M_{rel} and DR. Also note that a letter s next to a case number denotes a swirling case.

V. Results and Discussion

A. Shock Structure (Nonswirling, No Fuel Injection)

The shock structure of a simple underexpanded supersonic flow is shown schematically in Fig. 6. As can be seen, the structure comprises a shock-cell unit that gets repeated periodically to form a shock-cell train. This unit can be described as follows. Axial underexpanded flow undergoes an expansion fan and turns outward. The free-jet boundary adapts accordingly and turns outward as well. Passing again through the expansion fan, the outward flow turns back to axial. As the expansion fan meets the boundary, it reflects into a compression fan that coalesces later into the intercepting shock wave. The annular flow adjacent to boundary turns inward through the compression fan, and the boundary again adapts by turning inward as well. For slightly underexpanded nozzles, this intercepting shock reflects directly into a reflected shock at the centerline, forming the familiar diamond configuration. However, as the pressure ratio across the nozzle is increased, this reflection no longer takes place at the centerline, and a Mach disk is formed. The reflected shock turns the inward annular flow back to the axial direction. Since the Mach disk maintains the axial direction of core flow, the entire flow is now axial again. As the reflected shock impinges on the flow free

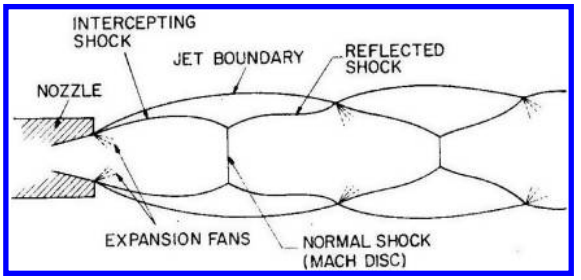

Fig. 6 Schematic of shock structure of nonswirling highly underexpanded nozzle flow [2].

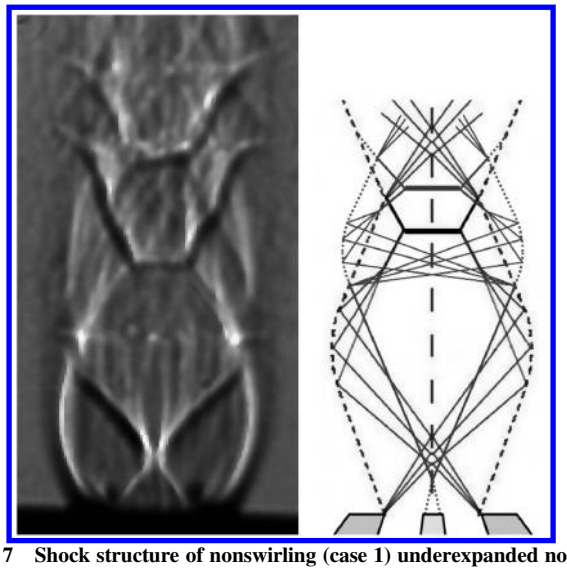

Fig. 7 Shock structure of nonswirling (case 1) underexpanded nozzle airflow in presence of nonrecessed coaxial injection system with no fuel injection.

boundary, it reflects into an expansion fan, starting another shock-cell unit. The repetition of units is continued until viscous effects become predominant and this structure is no longer observed.

In the presence of a coaxial injection system, the shock structure differs significantly from the simple one described above. Figure 7 shows a schlieren image as well as a schematic of the shock structure of free nozzle flow in the presence of a nonrecessed coaxial injection system with no fuel injection. Two distinct substructures are identifiable from the schlieren image and highlighted in the schematic. The first substructure is the simple nozzle-rim structure discussed above. A new substructure is generated due to the existence of the coaxial injection system. It should be noted here that both substructures are not fully independent of each other. The presence of each affects the other. This interaction is not indicated on the schematic in Fig. 7, however, for easier understanding of the newly introduced substructure of the injection system. Indicated here is how each structure would propagate if fully independent of the other. From this point forward, the nozzle-rim and injection-system substructures will be denoted as *primary* and *secondary* shock structures, respectively, in this study.

The secondary structure starts with the airflow generating an inner conical boundary that completes the cone-frustum shape of the fuel system tip. At the centerline, the flow collapses into itself, generating a conical shock wave that turns the flow back to parallel. This shock wave impinges on the outer flow boundaries shortly downstream of the impingement location of the nozzle-rim expansion fan. The outer boundaries are altered by the impingement of that conical shock as observed from Fig. 7. The shock reflects into an expansion fan that creates its own compression fan, intercepting shock, Mach disk, and reflected shock, similar to the primary structure. Both Mach disks of the primary and secondary structures appear distinctly in Fig. 7.

The effect of coaxial fuel injection is shown in Fig. 8. Helium is used as the fuel stimulant. As observed, the secondary shock structure is altered slightly. A shear layer develops in place of the former inner conical boundaries of airflow. Because of the presence of helium, the shear layer does not converge to a sharp point at the centerline. Moreover, due to the curved shape of this shear layer, the airflow undergoes a gradual compression through a compression fan, which collapses later into a shock wave that generates the secondary shock substructure.

B. Validation of Numerical Code

Numerical simulations of the flowfield have been performed in this study, in addition to the experimental investigation, to broaden the scope of analysis of the latter and provide the desired quantification of certain flowfield parameters. For example, the schlieren technique is incapable of quantifying the different components of Mach number. Therefore, the numerical results are used to provide the missing data needed for examining the air/fuel shear layer and propagation of swirl throughout flowfield.

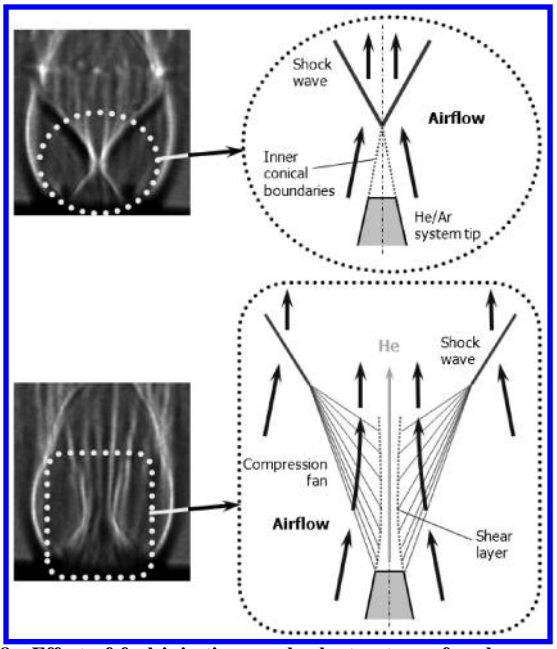

Fig. 8 Effect of fuel injection on shock structure of underexpanded nozzle flow.

Code validation was performed by comparing the numerical centerline static-pressure trace within the near-field supersonic flowfield of case 0s1 to corresponding experimental data (see Figs. 4c and 5a). The centerline static pressure was measured experimentally within the near-field supersonic flowfield by inserting a knife-edge circular disc vertically inside the flow (see Fig. 5b). The disc has an outer diameter of $0.9D$ with a 0.5 mm internal channel for transferring the static-pressure signal to a 100 psi pressure transducer of 0.15 psi (0.01 bar) full-scale accuracy. The knife edge of the circular disc serves for cutting through the supersonic flow with minimum disturbance on the flat side, which is aligned with the nozzle centerline. It can be seen from Figs. 4c and 5 that the numerical code generally overpredicts the static pressure. This trend was observed to persist over the region of interest, which is composed of the subsonic flow inside the nozzle and the near-field supersonic flow up to $5D$ downstream of the nozzle exit. A maximum error of 7% was observed, which shows good agreement and was considered acceptable for the scope of this study.

In light of the aforementioned code-validation comparison it can be concluded the Baldwin–Lomax turbulence model is capable of predicting free supersonic swirling flows with good accuracy. This negates the common generic belief that this model poorly predicts swirling flows, which might be true under subsonic conditions but not under supersonic conditions, based on the findings of this study. Had the modified versions of the Baldwin–Lomax model been available in the FASTRAN-code library, better prediction accuracy might have been achieved. The reader is referred to previous studies conducted by the authors [31,32], in which the Baldwin–Lomax model was successfully implemented in simulating confined supersonic flows using the hybrid LES/RANS FASTRAN code.

C. Supersonic Flowfield

The main objective of this current study is to analyze how swirl affects the supersonic flowfield and shock strength in underexpanded airflow with coaxial fuel injection. Before beginning the analysis, an important fact should be recalled here pertaining to the subsonic flowfield inside nozzle. This flow is blind to the atmospheric backpressure outside, due to the sonic barrier at the throat. In other words, the subsonic flow does not adapt to the backpressure by fixing the throat static pressure at a certain value, regardless of nozzle reservoir pressure. However, once the flow exits the nozzle, it is highly sensitive to the backpressure. If the flow pressure is different from the backpressure, the former has to be matched to the latter, which results in the formation of a shock structure in the supersonic flowfield outside the nozzle. Convergent nozzles always generate underexpanded jets if the backpressure is atmospheric. The superatmospheric throat static pressure dictates how much expansion is still needed and consequently controls the geometry and strength of the formed shock structure, as explained earlier in the analysis of Fig. 6.

Based on the findings of Adamson and Nicholls [2], Lewis and Carlson [3], and Crist et al. [4], the axial position of the first Mach disk (relative to nozzle exit) increases with reservoir pressure. In light of the present study, this statement should be corrected to state that the axial position of the first Mach disk is affected by both throat static pressure and degree of swirl. Before explaining why this correction is necessary, consider a new case, to be called 0s2, which is a swirling case like 0s1 but has the lower reservoir pressure of case 0. All three cases have the same inlet total temperature of 300 K. Figure 9 shows the schlieren images of cases 0, 0s2, and 0s1. The horizontal white line highlights the differences in positions of the first Mach disk in cases 0s2 and 0s1 relative to case 0. It can be observed that the reservoir pressure is not the sole parameter that controls the position of the first Mach disk. Although cases 0 and 0s2 have the same reservoir pressure, the latter has an axially compact shock

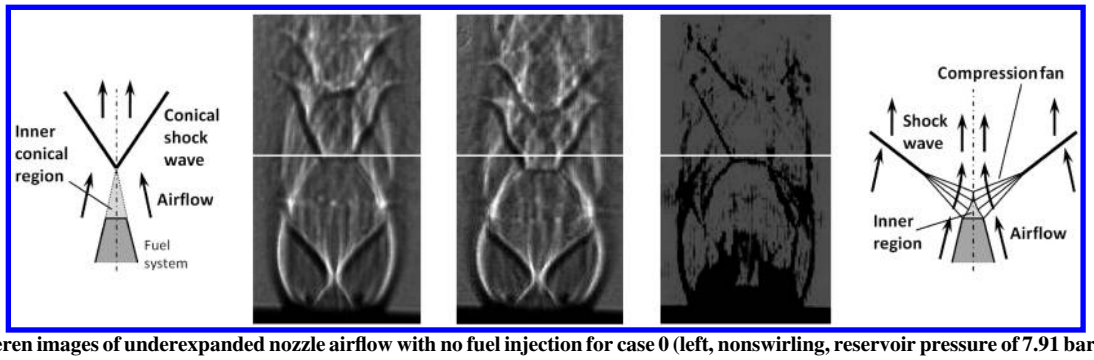

Fig. 9 Schlieren images of underexpanded nozzle airflow with no fuel injection for case 0 (left, nonswirling, reservoir pressure of 7.91 bar), 0s2 (middle, swirling, reservoir pressure of 7.91 bar), and 0s1 (right, swirling, reservoir pressure of 8.82 bar).

structure. This does not apply for cases 0 and 0s1, which have different reservoir pressures yet similar positions of the first Mach disk. Only the comparison of cases 0s2 and 0s1 reveals the expected trend, in which increasing reservoir pressure results in an axial stretching of shock structure. The effect of swirl explains those unexpected behaviors. Swirling flowfields have two unique features that are absent in nonswirling flowfields. First, the flow is pushed radially outward by the Coriolis effect. Second, a swirling jet has two velocity gradients (axial and tangential) across its shear layer with the ambient air, which contributes to increasing the jet diameter, as compared with a nonswirling jet with an axial velocity gradient only. The fact that swirl increases the jet diameter is confirmed in Fig. 9, in which it can be observed that the jet diameter within the first shock cell is slightly larger in case 0s2 than it is in case 0. The larger diameter is accompanied by an axially compact shock structure, which appears to be a common feature of supersonic and subsonic swirling jets. Thus, it can be concluded that the effects of swirl and nozzle reservoir pressure interfere destructively from the point of view of shock-structure axial compactness. Increasing reservoir pressure stretches the shock structure axially (case 0s2 to 0s1), whereas swirl shrinks it (case 0 to 0s2). This explains why the axial positions of the first Mach disk in cases 0 and 0s1 are almost identical. It should be noted here that the effects of swirl and nozzle reservoir pressure interfere constructively from the point of view of jet radial expansion. Note from Fig. 9 that the flowfield of case 0s1 has a slightly larger diameter than that of case 0s2.

To quantify the effects of swirl and nozzle reservoir pressure in more detail, Fig. 10 shows the axial distributions of computed centerline static pressure in the supersonic flowfields of cases 0, 0s2, and 0s1. Multiple observations can be made from Fig. 10. The flat segments of nearly constant static pressure immediately downstream of the nozzle exit represent the confined inner region observed in Fig. 9 and discussed in the analysis of Fig. 7. Very low subsonic Mach numbers exist inside this region, which explains why its centerline static pressure is almost equal to the total pressure of surrounding supersonic airflow. The presence of the nozzle-rim expansion fan is noticed downstream of the inner region. Subatmospheric pressures are reached as the flow passes through the expansion fan twice (refer back to the analysis of Fig. 7 for more details). Note that case 0s1 expands from 5.4 to 0.4 atm, whereas case 0 expands only from 4.0 to 0.5 atm. This shows that the combination of swirl and higher reservoir pressure results in a greater expansion fan in case 0s1, which is in agreement with the findings of a previous study conducted by the authors [27]. The considerably larger dark region observed immediately downstream of the nozzle exit in the schlieren image of case 0s1 is, in fact, a greater nozzle-rim expansion fan.

The realm of the first primary and secondary shock cups is identified in Fig. 10 by the recovery from the minimum subatmospheric pressure to a local maximum of superatmospheric pressure. It can be seen that the first primary shock cup is approached at $z/D \approx 1.45$ in case 0, ≈ 1.4 in case 0s1, and ≈ 1.25 in case 0s2. This agrees with the qualitative analysis made earlier in Fig. 9. The effect of swirl is evident in the upstream shift from 1.45 to 1.25, and the effect of nozzle reservoir pressure is obvious in the downstream shift from 1.25 to 1.4. Both effects interfere destructively, yielding almost the same axial compactness of shock structure in cases 0 and 0s1.

The strength of the shock structure can also be quantified from Fig. 10. Although the structure of case 0 recovers 0.70 atm, that of case 0s2 recovers only 0.64 atm. The structure of case 0s1, on the other hand, recovers 0.89 atm. Thus, it can be concluded here that the application of swirl at matched nozzle reservoir pressure weakens the shock structure as expected. It was shown in the work of Abdelhafez and Gupta [27] that both nonswirling and swirling flowfields start off with the same level of energy upstream of the nozzle, but the latter dissipates more energy than the former in friction losses inside the nozzle. Consequently, the swirling throat flow has a smaller potential of pressure energy to dissipate through shock structure.

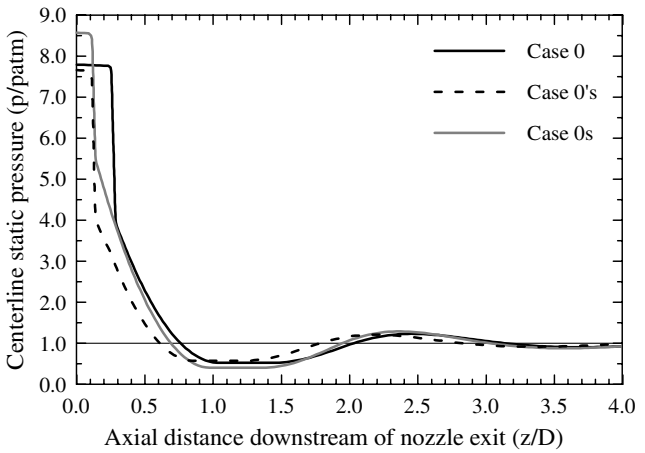

Fig. 10 Axial variation of centerline static pressure within first two shock cells in cases 0 (nonswirling, reservoir pressure of 7.91 bar), 0s2 (swirling, reservoir pressure of 7.91 bar), and 0s1 (swirling, reservoir pressure of 8.82 bar).

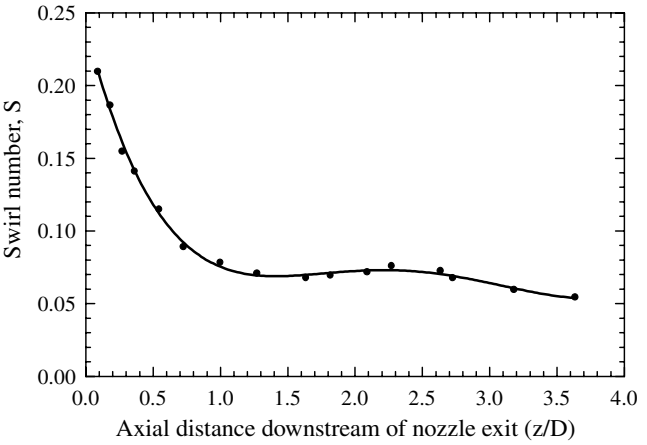

Fig. 11 Axial variation of supersonic swirl number within first two shock cells in case 0s1.

The application of swirl at matched mass flow, on the other hand, results in a stronger structure, because of the greater potential of pressure energy at the throat.

Having analyzed the effect of swirl on the shock structure, the analysis extends now to examine the supersonic swirl number. Figure 11 shows the axial variation of supersonic swirl number within the first two shock cells of case 0s1. The swirl number was computed at select sections inside the nozzle using the correlation [23]

$$S = \frac{\int_{R_i}^{R_o} v_a v_t r^2 \, \mathrm{d}r}{R_o \int_{R_i}^{R_o} v_a^2 r \, \mathrm{d}r} \tag{3}$$

where v_a and v_t are the numerically obtained axial and tangential velocity components, respectively. It can be observed that the supersonic swirl number decreases in the axial direction. This is attributed to a substantial increase in axial momentum as the flow expands and accelerates. A minimum swirl number of 0.07 is observed at z/D of about 1.4, before the swirl number experiences a slight local increase between z/D of 1.4 and 2.7. Recall from Fig. 10 that the realm of the first primary and secondary shock cups in case 0s1 starts at $z/D \approx 1.4$. To understand why the supersonic swirl number experiences a slight local increase within the shock cups, it should be noted that the axial and tangential velocity components behave very differently through shock cups. Figure 12 helps explain this statement. Depicted is a three-dimensional schematic of shock structure, showing the orientation of v_a and v_t with respect to the main features: i.e., Mach disk and intercepting and reflected shocks. It can be easily visualized how v_a is always perpendicular to the Mach disk. Moreover, both intercepting and reflected shocks are oblique with respect to v_a. For these two reasons, the axial Mach number and momentum undergo significant reductions through shock structure. The tangential velocity component, on the other hand, is always parallel to all features of the shock structure. According to the fundamentals of gas dynamics, the velocity component parallel to the plane of a shock wave is preserved through the shock and experiences no change. Combining the behaviors of v_a and v_t through shock structure, one can easily explain the small local increase in swirl number within the realm of shock cups, especially when one recalls that the swirl number is proportional to the ratio of average tangential to axial momenta.

D. Effect of Relative Mach Number M_{rel}

Having attained a good understanding of the effect of swirl on the supersonic flowfield, the analysis proceeds to examine the effect of fuel injection at different relative Mach numbers. Recall that M_{rel} is defined here as the ratio of $v_{air} - v_{fuel}$ to the average speed of sound, where v_{air} is the throat velocity of air, and v_{fuel} is the injection velocity of fuel, since fuel is injected coaxially at the nozzle throat (i.e., no recess) in all of the following analyses. Also recall that the close values of sonic air velocity under nonswirling and swirling conditions allowed for examining the same values of relative Mach number and air/fuel DR with and without swirl. Another very important detail to be pointed out here is that swirl is imparted to the air at matched mass flow from this point forward; i.e., all swirling cases have the same mass flow rate of the nonswirling cases (175 g/s). This implies that the swirling cases have the elevated nozzle reservoir pressure of 8.82 bar. Matching of air mass flow allows for a fair comparison between the different case pairs, primarily from the point of view of mixture fractions and mixedness.

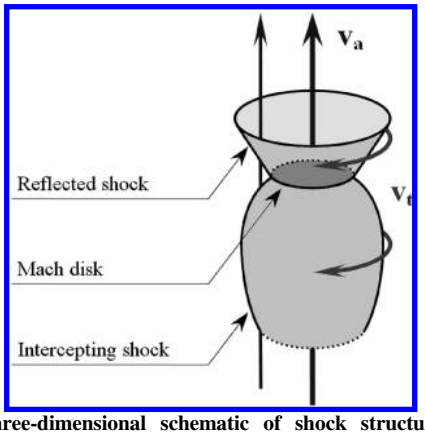

Fig. 12 Three-dimensional schematic of shock structure showing orientation of axial and tangential velocity components with respect to Mach disk and intercepting and reflected shocks.

The effect of M_{rel} is examined in case pairs 1–13 given in Table 1. Case pairs 1–9 span the M_{rel} range 0.44–0.26 experimentally. Case pairs 1 (range begin), 5 (range middle), and 9 (range end) were selected to be examined both experimentally and numerically, to optimize the parameters of the numerical code for best agreement with the experimental results. The experimental range is extended numerically to −0.48 in case pairs 10–13. Case pair 11 represents a unique condition, in which fuel is injected at the throat velocity of air, resulting in M_{rel} of zero. Case pairs 12 and 13 represent the extreme situations, in which fuel is injected at velocities higher than the throat velocity of air. The corresponding values of M_{rel} are indicated here without neglecting their negative signs, to highlight the unique nature of those two case pairs.

Keeping all airflow properties constant, the flow rate of fuel (simulated by helium) was changed to induce different fuel velocities and thus multiple values of M_{rel}. The injection Mach number of helium was kept below 0.3 (except in case pairs 12 and 13), to maintain a constant helium density and to avoid compressibility effects on the helium side of the air/helium shear layer. The resulting DR was about 35.5 for most cases. The supply pressure of helium was carefully selected for each case pair to match the total pressures of helium and air at injection.

Figure 13 shows the effect of M_{rel} at constant DR. The experimental results (schlieren images) are depicted in Fig. 13a, and Fig. 13b shows the numerical results in the form of Mach number profiles. The nonswirling cases are depicted in the top row of each figure, and the bottom row contains the swirling cases. The values of M_{rel} and injection Mach number of each case pair are indicated at the top of its column.

The most remarkable observation to be made from Fig. 13 is that the air/fuel shear layer initiates with a negative angle that transforms later to positive. In other words, the cross-sectional area of core flow converges initially to a minimum value before propagating divergently as expected. Figure 14 helps explain this observation. Shown are the axial variations of computed centerline Mach number for different values of M_{rel} under nonswirling conditions. Note that subsonic injection is implemented throughout the analysis of M_{rel}. However, the centerline Mach numbers are observed to increase from the subsonic injection values to supersonic maxima of 1.75–2.10. The only possible way for the subsonic core flow to expand to supersonic speeds is through the fuel/air shear layer resembling a convergent–divergent nozzle. This can only be achieved if the cross-sectional area of the core flow initially converges to a throat before diverging again. The creation of a throat allows the core flow to transition from subsonic to supersonic speeds. To attain further understanding of the location of the core-flow throat within the flowfield, Fig. 15 shows how the axial position of this throat varies with M_{rel}. Note that at high M_{rel} (i.e., low injection velocities) the core flow propagates axially for about $0.5D$ with a negative shear angle. The throat of core flow, however, approaches the nozzle exit at low M_{rel} (high injection velocities), and negative-shear-angle propagation is confined to an axial distance of $0.25D$ at the highest injection velocity examined here.

It can be concluded here from the analysis of the core-flow throat that fuel injected at low subsonic Mach numbers (high M_{rel}) has to propagate for longer axial distances with a negative shear angle before the fuel-rich core flow reaches a throat after which it propagates supersonically. This is advantageous from two aspects. First, increasing the distance between the core throat and injection point allows for more mixing to take place across a supersonic/subsonic shear layer, which is significantly more effective than the fully supersonic one downstream of the core throat. The second advantage of low injection Mach numbers is that a negative-angled shear layer

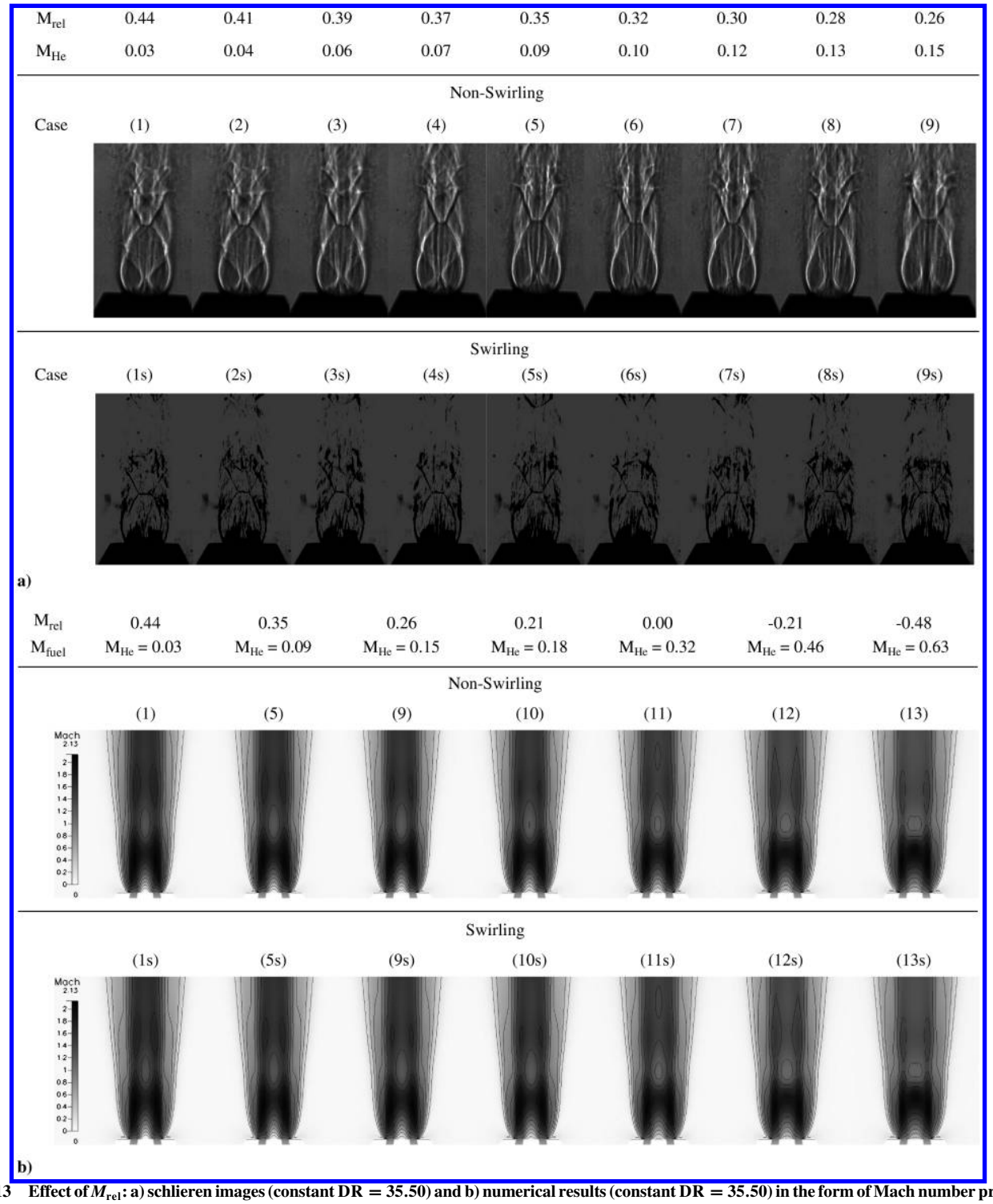

Fig. 13 Effect of M_{rel}: a) schlieren images (constant DR = 35.50) and b) numerical results (constant DR = 35.50) in the form of Mach number profiles.

propagates with a radially inward component, which allows it to confine the fuel-rich core flow more effectively. This core is thus consumed more rapidly by the growing shear layer.

Another notable advantage of the presence of a negative shear angle downstream of the injection point can be observed in the strength of the shock structure. As shown schematically in Fig. 16, the inner conical boundaries and conical shock wave, which initiate the secondary shock substructure in the absence of fuel injection, are replaced by a compression fan that is generated by the curved profile of the negative shear angle at subsonic injection Mach numbers. This fan allows for a gradual compression of the airflow. Although the fan eventually collapses into a shock wave, the strength of this wave is significantly lower than the conical one with no fuel injection. If M_{rel} is decreased (by increasing injection Mach number), the throat of core flow approaches the injection point, as mentioned earlier. Consequently, the negative shear angle and its compression fan diminish gradually. At the extreme of sonic injection a positive shear angle exists right from the start, accompanied by a strong shock at the injection point. This results in a stronger shock structure. Figure 13b confirms this discussion. Note that the average Mach number within the second shock cell is significantly reduced as the injection Mach number increases and M_{rel} decreases.

E. Effect of Air/Fuel Density Ratio

Having analyzed the effect of relative Mach number, the analysis proceeds to examine the effect of air/fuel DR at constant M_{rel}. DR is defined here as the ratio of throat density of air to injection density of

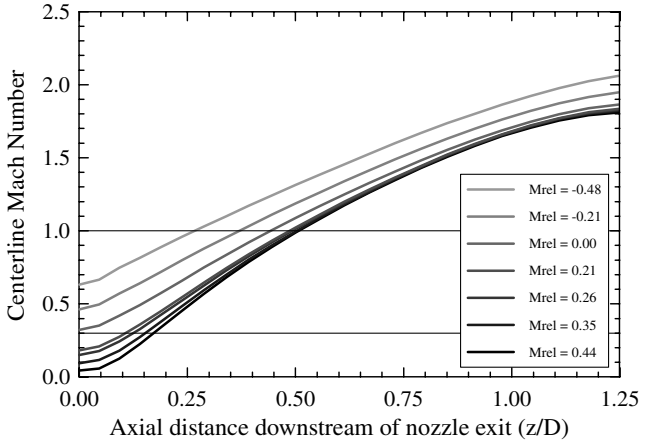

Fig. 14 Axial variations of centerline Mach number for different values of M_{rel} under nonswirling conditions.

fuel. Also recall that the close values of sonic air velocity under nonswirling and swirling conditions allowed for examining the same values of DR with and without swirl. Another very important detail to be pointed out again here is that swirl is imparted to air at matched mass flow; i.e., all swirling cases have the same mass flow rate of the nonswirling cases (175 g/s). This implies that the swirling cases have the elevated nozzle reservoir pressure of 8.82 bar.

The effect of DR is examined in case pairs 14–23 given in Table 1. Case pairs 15–21 span the DR range of 12.68–4.33 experimentally. Case pairs 15 (range begin), 18 (range middle), and 21 (range end) were selected to be examined both experimentally and numerically, to optimize the parameters of numerical code for best agreement with the experimental results. The experimental range is extended numerically from both sides. Case 14 examines a DR of 35.5, and case pairs 22 and 23 have DRs of 3.24 and 2.29, respectively. Note that case pairs 10 (from M_{rel} analysis) and 14 are identical, as they have the same fuel simulant (helium), M_{rel}, and DR.

Keeping all airflow properties constant, fuel was simulated by different inert-gas mixtures (helium, argon, and krypton). The mixture composition is varied to change mixture density and, consequently, DR. To maintain a constant M_{rel} of 0.21 throughout this analysis, the injection velocity was adjusted to account for the changes in a_{fuel} due to the varying injectant composition. The supply pressure of fuel was carefully selected for each case pair to match the total pressures of fuel and air at injection. Compressible injection is used throughout this analysis, except for case pair 14, which is copied over from the M_{rel} analysis. Case pair 23 represents the extreme conditions, in which fuel is injected at its sonic velocity: i.e., the injection system is choked.

Figure 17 shows the effect of DR at constant M_{rel}. The experimental results (schlieren images) are depicted in Fig. 17a, and

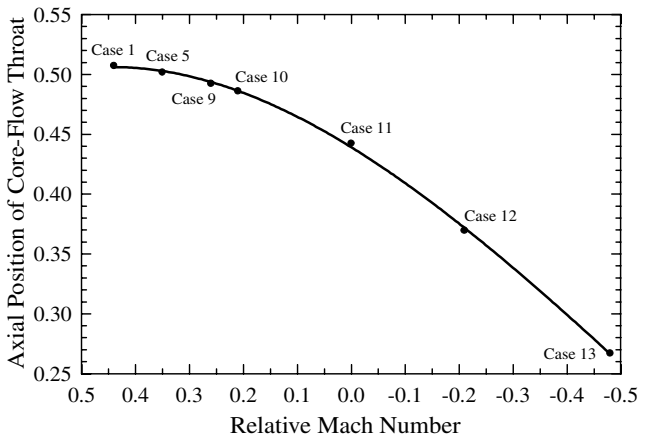

Fig. 15 Variation of axial position of core-flow throat with M_{rel}.

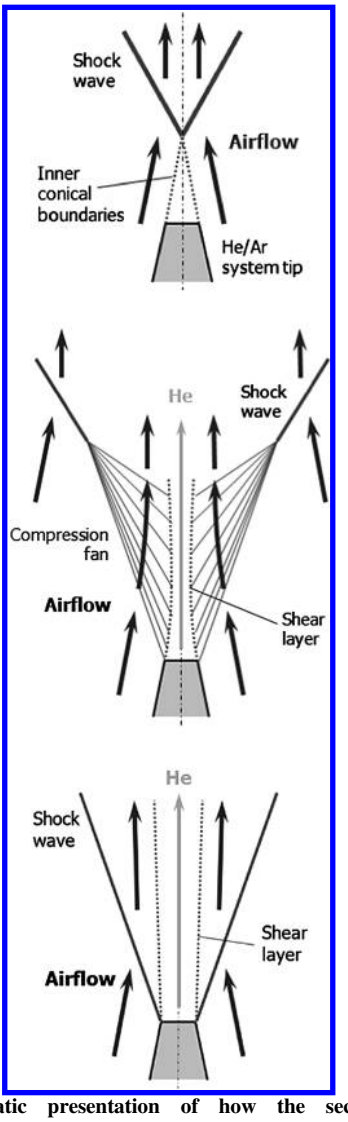

Fig. 16 Schematic presentation of how the secondary shock substructure initiates; no fuel injection (left), high M_{rel} (middle), and low M_{rel} (right).

Fig. 17b shows the numerical results in the form of Mach number profiles. The nonswirling cases are depicted in the top row of each figure, and the bottom row contains the swirling cases. The values of DR and injection Mach number of each case pair are indicated at the top of its column, together with the composition of fuel simulant.

In light of the comprehensive M_{rel} analysis, the effect of DR will be analyzed here in a concise fashion. It can be observed from Fig. 17 that the air/fuel shear layer again initiates with a negative angle that transforms later to positive. Consequently, the cross-sectional area of core flow converges initially to a throat before propagating divergently. This allows the core flow to accelerate from the subsonic Mach numbers of injection to supersonic maxima of 1.84–2.13 in Fig. 18. The variation of axial position of core throat with DR is shown in Fig. 19. Note that at high DR the core flow propagates axially for about 0.5D with a negative shear angle. However, at a DR of 2.29, the throat of core flow is exactly at the nozzle exit and negative-shear-angle propagation is completely absent. The effect of DR on shock-structure strength is observed in Fig. 17b. Note again that the transition from negative to positive shear angles results in stronger shock structure at low DR, as evidenced in the decreasing average Mach number within the second shock cell.

F. Shear-Layer Growth

The analyses of M_{rel} and DR revealed how the angle of the air/fuel shear layer critically affects both the shock structure and mixing. The

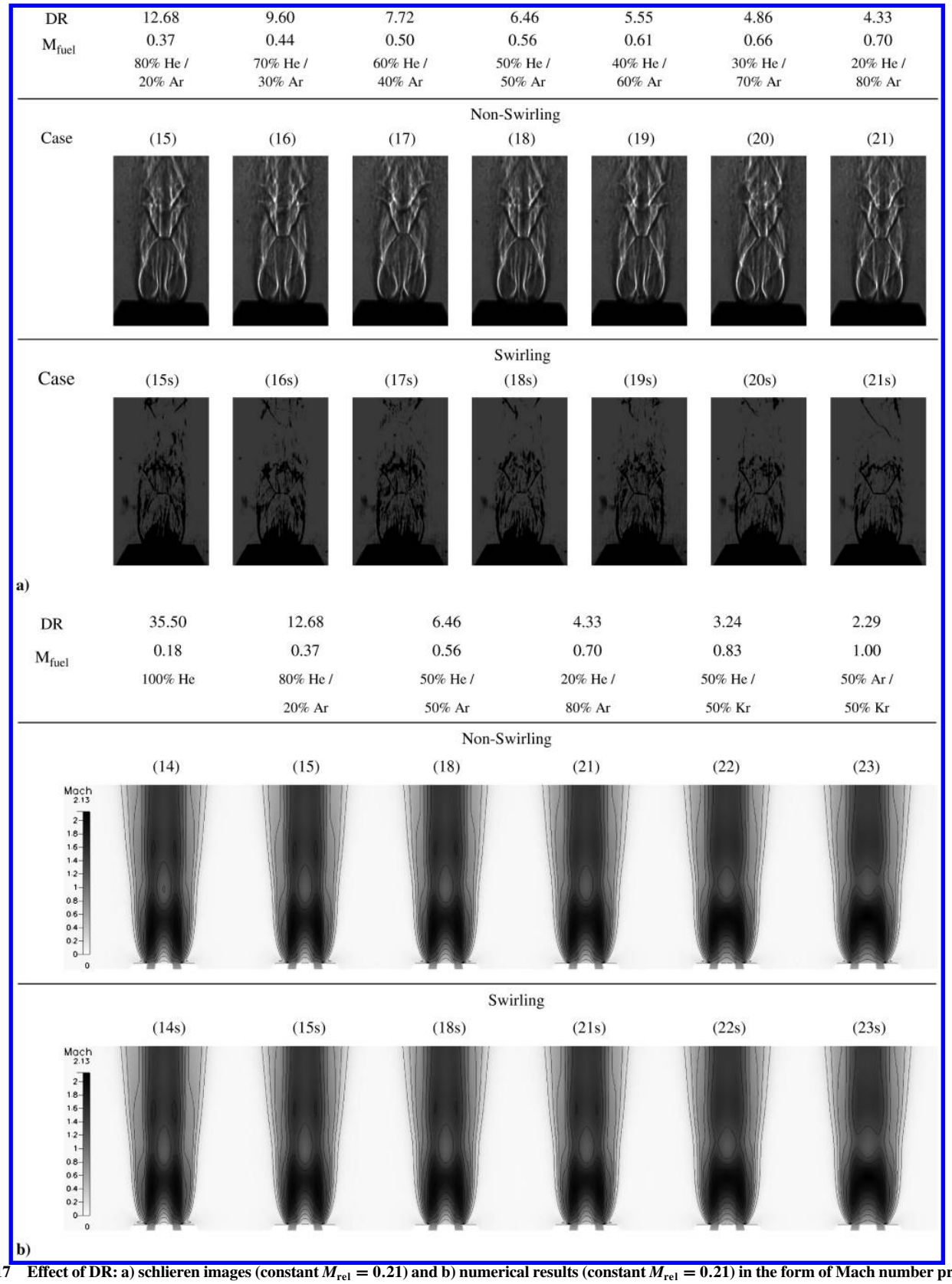

Fig. 17 Effect of DR: a) schlieren images (constant $M_{rel} = 0.21$) and b) numerical results (constant $M_{rel} = 0.21$) in the form of Mach number profiles.

following analysis is thus dedicated to attaining a better understanding of the shear-layer growth, which is another very important parameter. An analysis of the shear-layer thickness is conducted here, following the same roadmap of Papamoschou and Roshko [13]. They defined a convective frame of reference that incorporates the effect of flow compressibility and accounts for different speeds of sound on both sides of the shear layer. Figure 20 compares this convective frame of reference to the stationary (traditional) one. Note that the former moves with the flow at the convective wave velocity v_c. The mainstream Mach numbers on both sides of the shear layer transform to this new frame of reference as follows:

$$M_{c_{air}} = \frac{v_{air} - v_c}{a_{air}} \quad \text{and} \quad M_{c_{fuel}} = \frac{v_c - v_{fuel}}{a_{fuel}} \tag{4}$$

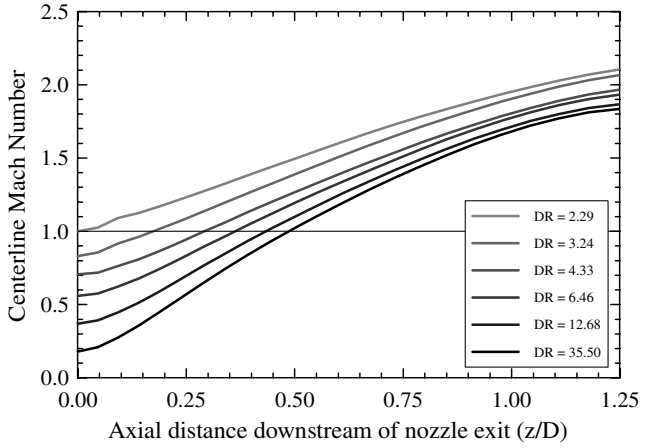

Fig. 18 Axial variations of centerline Mach number for different values of DR under nonswirling conditions.

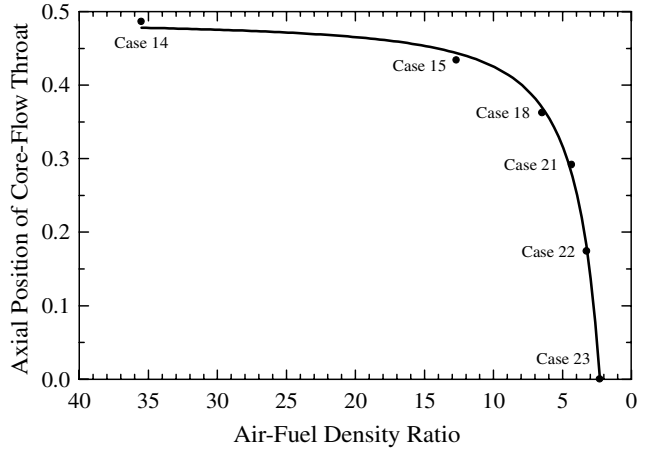

Fig. 19 Variation of axial position of core-flow throat with DR.

where M_c stands for convective Mach number. Both values are considerably close, and they always have the same sign, since v_c always lies somewhere between v_{air} and v_{fuel}. If a streamline is traced across the shear layer, as seen in Fig. 20, a point has to be met, where the

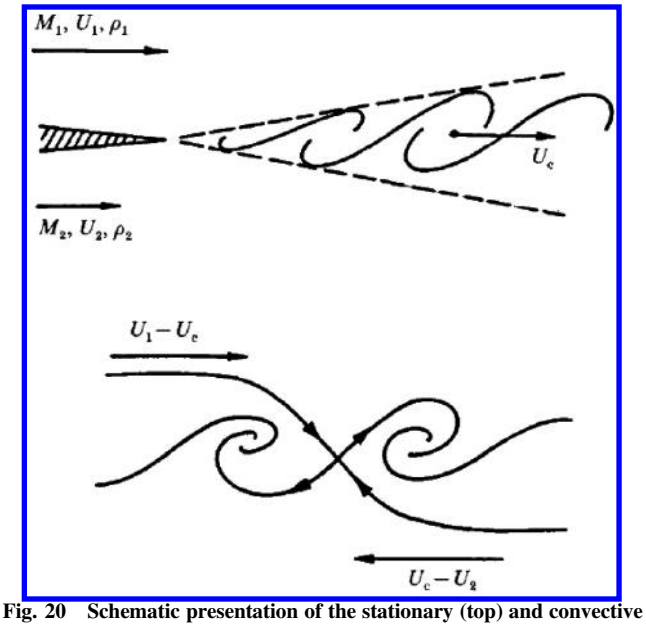

Fig. 20 Schematic presentation of the stationary (top) and convective (bottom) frames of reference with sketches of streamlines (Papamoschou and Roshko [13]).

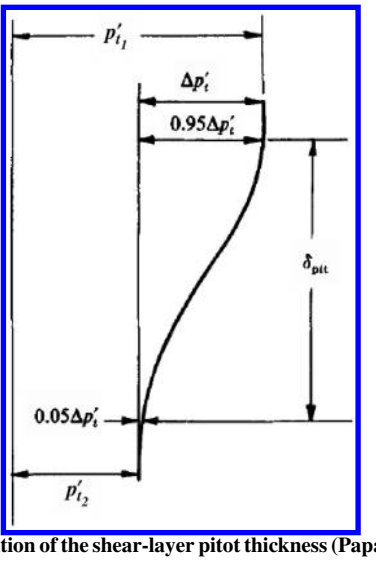

Fig. 21 Definition of the shear-layer pitot thickness (Papamoschou and Roshko [13]).

local velocity is v_c on an absolute scale but zero (stagnation) on the convective one. This stagnation point forces the equilibrium of total pressures on both sides of the shear layer; that is,

$$p_{air}\left(1+\frac{\gamma_{air}-1}{2}M_{c_{air}}^2\right)^{\frac{\gamma_{air}}{\gamma_{air}-1}} = p_{fuel}\left(1+\frac{\gamma_{fuel}-1}{2}M_{c_{fuel}}^2\right)^{\frac{\gamma_{fuel}}{\gamma_{fuel}-1}} \quad (5)$$

Substituting from Eq. (4) into Eq. (5), the convective wave velocity can be solved for by trial and error. Backsubstitution in Eq. (4) then yields the individual convective Mach numbers of air and fuel. The effect of convective Mach number on shear-layer thickness can thus be quantified, which is a direct indication of how the degrees of compressibility of mainstreams on both sides of the shear layer affect its growth rate. Shear-layer thickness is determined as follows. Consider the shear layer shown schematically in Fig. 21. A *pitot thickness* δ_{pit} is defined after Papamoschou and Roshko [13] as the width of total-pressure profile from 5 to 95% of the difference of mainstream values. The parameters p, γ, v, and a of air and fuel mainstreams are thus calculated at the end points of δ_{pit}.

The analysis of the shear-layer thickness is carried out here on all the numerical cases given in Table 1, since their simulations contain all of the necessary data. The axial positions $z/D = 0.1$ and 1.0 were selected in each case. Before constructing the final plot of δ_{pit} versus M_c, 24 additional simulations were conducted to replicate the 12 numerical case pairs of Table 1 under incompressible conditions while maintaining their individual velocity and density ratios. The analysis of the shear-layer thickness was applied to the attained incompressible flowfields at $z/D = 0.1$ and 1.0 as well. The ratio of

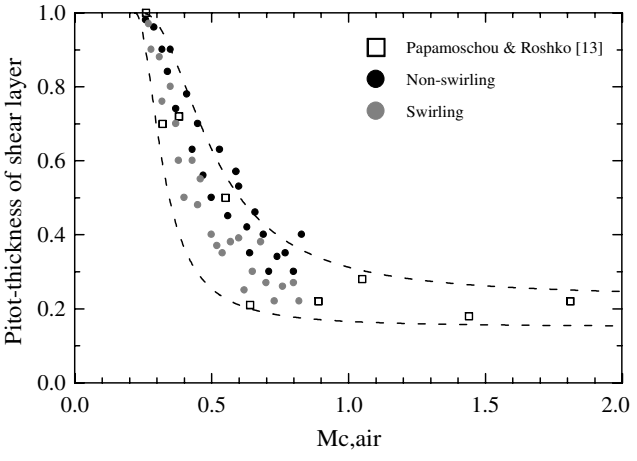

Fig. 22 Normalized pitot thickness of the shear layer versus $M_{c,air}$.

compressible-to-incompressible shear-layer thicknesses was finally calculated for all of the 24 numerical cases at hand. Figure 22 is the fruit of this effort. The normalized pitot thickness of the shear layer is plotted versus air convective Mach number. All data points fall in the Mach number range of 0.25–0.83. The findings of Papamoschou and Roshko [13] are also included. Good qualitative agreement is observed, since most data points of this current study fall within the dashed lines that represent bounding envelopes of the results of Papamoschou and Roshko. A very important conclusion to be made from Fig. 22 is that the normalized shear-layer pitot thickness decreases with the application of swirl. It should be noted, however, that this reduction occurs in the normalized thickness and not the absolute one. As a matter of fact, it was noticed throughout the computations of Fig. 22 that the absolute value of the shear-layer thickness increases slightly with swirl, which agrees with the findings of Cutler et al. [20], Cutler and Levey [21], and Levey [22]. The controversy is caused here by the fact that the thickness of an incompressible shear layer was found to increase more with swirl than that of a compressible shear layer.

VI. Conclusions

This work provided an experimental/numerical investigation, in which the effect of imparting swirl to underexpanded supersonic-nozzle airflow on the shock structure was examined. Matched mass flow conditions were considered. A convergent nozzle with swirling capabilities was used to generate the underexpanded airflow. Fuel was injected coaxially at the nozzle throat. Nonreacting conditions were considered, in which in the fuel was simulated by mixtures of helium, argon, and krypton inert gases. Analyses were made of the effects of relative Mach number and density ratio across air/fuel shear layer. The effects of these parameters on the shock structure were investigated under both nonswirling and swirling conditions. The following conclusions were made:

1) The effects of swirl and nozzle reservoir pressure interfere destructively from the point of view of shock-structure axial compactness. Increasing reservoir pressure stretches the shock structure axially, whereas swirl shrinks it. On the other hand, both effects interfere constructively from the point of view of radial jet expansion; both result in greater jet diameter.

2) The application of swirl at matched reservoir pressure weakens the shock structure. The swirling throat flow is less underexpanded and has a smaller potential of pressure energy to dissipate through shock structure. The application of swirl at matched mass flow, on the other hand, results in a stronger structure, because the throat flow is more underexpanded and has a greater potential of pressure energy at the throat.

3) Fuel injected at low subsonic Mach numbers has to propagate initially with a negative shear angle. In other words, the cross-sectional area of fuel-rich core flow converges first, before this core flow reaches a throat after which it propagates supersonically. This behavior is advantageous, as it results in reduced shock-structure strength.

Acknowledgments

This work was supported by the Space Vehicle Technology Institute, jointly funded by NASA, U.S. Department of Defense, and U.S. Air Force within the NASA Constellation University Institutes Project (CUIP), with Claudia Meyer as the Project Manager. This support is gratefully acknowledged. The simulation package CFD-GEOM, CFD-FASTRAN, and CFD-VIEW was provided by ESI-Group and CFD Research Corporation. This support is gratefully acknowledged. Assistance provided by Adam Kareem in data acquisition and analysis is much appreciated.

References

[1] Buckley, P. L., Craig, R. R., Davis, D. L., and Schwartzkopf, K. G., "The Design and Combustion Performance of Practical Swirlers for Integral Rocket/Ramjets," *AIAA Journal*, Vol. 21, No. 5, 1983, pp. 733–740. doi:10.2514/3.8141

[2] Adamson, T. C., Jr., and Nicholls, J. A., "On the Structure of Jets from Highly Underexpanded Nozzles into Still Air," *Journal of the Aero/Space Sciences*, Vol. 26, No. 1, Jan. 1959, pp. 16–24.

[3] Lewis, C. H., Jr., and Carlson, D. J., "Normal Shock Location in Underexpanded Gas and Gas-Particle Jets," *AIAA Journal*, Vol. 2, No. 4, April 1964, pp. 776–777. doi:10.2514/3.2409

[4] Crist, S., Sherman, P. M., and Glass, D. R., "Study of the Highly Underexpanded Sonic Jet," *AIAA Journal*, Vol. 4, No. 1, 1966, pp. 68–71. doi:10.2514/3.3386

[5] Gostintsev, Y. A., Zelentsov, V. V., Ilyukhin, V. S., and Pokhil, P. F., "Structure of Underexpanded Supersonic Swirling Gas Jet," *Fluid Dynamics*, Vol. 4, No. 5, Sept. 1969, pp. 158–162.

[6] Batson, J. L., and Sforzini, R. H., "Swirling Flow Through a Nozzle," *Journal of Spacecraft and Rockets*, Vol. 7, No. 2, 1970, pp. 159–163. doi:10.2514/3.29892

[7] Settles, G. S., "Supersonic Mixing Enhancement by Vorticity for High-Speed Propulsion," NASA Langley Research Center, NASA-CR-188920, Hampton, VA, Oct. 1991.

[8] Lee, K. H., Setoguchi, T., Matsuo, S., and Kim, H. D., "*Proceedings of the Institution of Mechanical Engineers, Part C (Journal of Mechanical Engineering Science)*, Vol. 218, No. 1, 2004, pp. 93–103. doi:10.1243/095440604322786974

[9] Lee, K. H., Setoguchi, T., Matsuo, S., and Kim, H. D., "Influence of the Nozzle Inlet Configuration on Underexpanded Swirling Jet," *Proceedings of the Institution of Mechanical Engineers, Part C (Journal of Mechanical Engineering Science)*, Vol. 220, No. 2, 2006, pp. 155–163.

[10] Murakami, E., and Papamoschou, D., "Experiments on Mixing Enhancement in Dual-Stream Jets," 39th AIAA Aerospace Sciences Meeting & Exhibit, Reno, NV, AIAA Paper 2001-0668, Jan. 2001.

[11] Brown, G. L., and Roshko, A., "On Density Effects and Large Structure in Turbulent Mixing Layers," *Journal of Fluid Mechanics*, Vol. 64, No. 4, 1974, pp. 775–816. doi:10.1017/S002211207400190X

[12] Winant, C. D., and Browand, F. K., "Vortex Pairing: The Mechanism of Turbulent Mixing-Layer Growth at Moderate Reynolds Number," *Journal of Fluid Mechanics*, Vol. 63, No. 2, 1974, pp. 237–255. doi:10.1017/S0022112074001121

[13] Papamoschou, D., and Roshko, A., "The Compressible Turbulent Shear Layer: An Experimental Study," *Journal of Fluid Mechanics*, Vol. 197, 1988, pp. 453–477. doi:10.1017/S0022112088003325

[14] Clemens, N. T., and Mungal, M. G., "Two- and Three-Dimensional Effects in the Supersonic Mixing Layer," 26th AIAA/SAE/ASME/ASEE Joint Propulsion Conference, Orlando, FL, AIAA Paper 90-1978, July 1990.

[15] Hermanson, J. C., and Winter, M., "Imaging of a Transverse Sonic Jet in Supersonic Flow," 27th AIAA/SAE/ASME/ASEE Joint Propulsion Conference, Sacramento, CA, AIAA Paper 91-2269, June 1991.

[16] Hall, J. L., Dimotakis, P. E., and Rosemann, H., "Experiments in Non-Reacting Compressible Shear Layers," 29th AIAA Aerospace Sciences Meeting, Reno, NV, AIAA Paper 91-0629, Jan. 1991.

[17] Miles, J. W., "On the Disturbed Motion of a Plane Vortex Sheet," *Journal of Fluid Mechanics*, Vol. 4, No. 5, 1958, pp. 538–552. doi:10.1017/S0022112058000653

[18] Chinzei, N., Masuya, G., Komura, T., Mukrami, A., and Kudou, K., "Spreading of Two-Stream Supersonic Turbulent Mixing Layers," *Physics of Fluids*, Vol. 29, No. 5, 1986, pp. 1345–1347. doi:10.1063/1.865698

[19] Menon, S., "Numerical Simulations of Supersonic Flows Past Generic SCRAMJET Flameholders," U.S. Air Force, Rept.. 434, Wright-Patterson AFB, OH, 1988.

[20] Cutler, A. D., Levey, B. S., and Kraus, D. K., "An Experimental Investigation of Supersonic Swirling Jets," 24th AIAA Fluid Dynamics Conference, Orlando, FL, AIAA Paper 93-2922, July 1993.

[21] Cutler, A. D., and Levey, B. S., "Vortex Breakdown in a Supersonic Jet," AIAA Paper 91-1815, June 1991.

[22] Levey, B. S., "An Experimental Investigation of Supersonic Vortical Flow," M.S. Thesis, School of Engineering and Applied Science, George Washington Univ., Washington, D.C., Sept. 1991.

[23] Gupta, A. K., Lilley, D. G., and Syred, N., *Swirl Flows*, Abacus Press, Kent, England, U.K., 1984.

[24] Cutler, A. D., Levey, B. S., and Kraus, D. K., "Near-Field Flow of Supersonic Swirling Jets," *AIAA Journal*, Vol. 33, No. 5, 1995, pp. 876–881. doi:10.2514/3.12362

[25] Linck, M., "Spray Flame and Exhaust Jet Characteristics of a Pressurized Swirl Combustor," Ph.D. Thesis, Univ. of Maryland, College Park, MD, May 2006.
[26] Baldwin, B. S., and Lomax, H., "Thin Layer Approximation and Algebraic Model for Separated Turbulent Flows," 16th AIAA Aerospace Sciences Meeting, Huntsville, AL, AIAA Paper 78-257, Jan. 1978.
[27] Abdelhafez, A., and Gupta, A. K., "Swirling Airflow Through a Nozzle: Choking Criteria," *Journal of Propulsion and Power* (submitted for publication).
[28] Courant, R., Friedrichs, K., and Lewy, H., "On the Partial Difference Equations of Mathematical Physics," *IBM Journal of Research and Development*, Vol. 11, No. 2, Mar. 1967, pp. 215–234.
[29] Claypole, T. C., and Syred, N., "The Effects of Swirl Burner Aerodynamics on NOx Formation," *18th Symposium (International) on Combustion*, Combustion Inst., Pittsburgh, PA, 1981, pp. 81–89.
[30] Abdelhafez, A., and Gupta, A. K., "Swirl Effects on Free Underexpanded Supersonic Airflow," 47th AIAA Aerospace Sciences Meeting and Exhibit, Orlando, FL, AIAA Paper 2009-1557, Jan. 2009.
[31] Abdelhafez, A., and Gupta, A. K., "Numerical Investigation of Oblique Fuel Injection in a Supersonic Combustor," 46th AIAA Aerospace Sciences Meeting and Exhibit, Reno, NV, AIAA Paper 2008-0068, Jan. 2008.
[32] Abdelhafez, A., Gupta, A. K., Balar, R., and Yu, K. H., "Evaluation of Oblique and Traverse Fuel Injection in a Supersonic Combustor," 43rd AIAA/ASME/SAE/ASEE Joint Propulsion Conference & Exhibit, Cincinnati, OH, July 2007, AIAA Paper 2007-5026.

K. Frendi
Associate Editor